Technical University of Denmark

DTU

Bandwidth and wavelength-tunable optical bandpass filter based on silicon microring-MZI structure

Ding, Yunhong; Pu, Minhao; Liu, Liu; Xu, Jing; Peucheret, Christophe; Zhang, Xinliang; Huang, Dexiu; Ou, Haiyan

DTU Library
Technical Information Center of Denmark

Bandwidth and wavelength-tunable optical bandpass filter based on silicon microring-MZI structure

Yunhong Ding,[1,2] Minhao Pu,[2] Liu Liu,[2] Jing Xu,[2] Christophe Peucheret,[2] Xinliang Zhang,[1] Dexiu Huang,[1,*] and Haiyan Ou[2]

[1]*Wuhan National Laboratory for Optoelectronics, School of Optoelectronics Science and Engineering, Huazhong University of Science and Technology, Wuhan, 430074, Hubei, China*
[2]*Department of Photonics Engineering, Technical University of Denmark, 2800 Kgs. Lyngby, Denmark*
*wnlo2@mail.hust.edu.cn

Abstract: A novel and simple bandwidth and wavelength-tunable optical bandpass filter based on silicon microrings in a Mach-Zehnder interferometer (MZI) structure is proposed and demonstrated. In this filter design, the drop transmissions of two microring resonators are combined to provide the desired tunability. A detailed analysis and the design of the device are presented. The shape factor and extinction ratio of the filter are optimized by thermally controlling the phase difference between the two arms of the MZI. Simultaneous bandwidth and wavelength tunability with in-band ripple control is demonstrated by thermally tuning the resonance offset between the two microring resonators.

References and links

1. Y. Yanagase, S. Suzuki, Y. Kokubun, and S. T. Chu, "Box-like filter response and expansion of FSR by a vertically triple coupled microring resonator filter," J. Lightwave Technol. **20**(8), 1525–1529 (2002).
2. M.-C. M. Lee and M. C. Wu, "Variable bandwidth of dynamic add-drop filters based on coupling-controlled microdisk resonators," Opt. Lett. **31**(16), 2444–2446 (2006).
3. J. Yao and M. C. Wu, "Bandwidth-tunable add-drop filters based on micro-electro-mechanical-system actuated silicon microtoroidal resonators," Opt. Lett. **34**(17), 2557–2559 (2009).
4. L. Chen, N. Sherwood-Droz, and M. Lipson, "Compact bandwidth-tunable microring resonators," Opt. Lett. **32**(22), 3361–3363 (2007).
5. B. Little, C. Sai, C. Wei, J. Hryniewicz, D. Gill, O. King, F. Johnson, R. Davidson, K. Donovan, C. Wenlu, and S. Grubb, "Tunable bandwidth microring resonator filters," in the 34th European Conference on Optical Communication, ECOC 2008, 1–2.
6. Z. Wang, S.-J. Chang, C.-Y. Ni, and Y. J. Chen, "A high-performance ultracompact optical interleaver based on double-ring assisted Mach-Zehnder interferometer," IEEE Photon. Technol. Lett. **19**(14), 1072–1074 (2007).
7. M. S. Rasras, D. M. Gill, S. S. Patel, K.-Y. Tu, Y.-K. Chen, A. E. White, A. T. S. Pomerene, D. N. Carothers, M. J. Grove, D. K. Sparacin, J. Michel, M. A. Beals, and L. C. Kimerling, "Demonstration of a fourth-order pole-zero optical filter integrated using CMOS processes," J. Lightwave Technol. **25**(1), 87–92 (2007).
8. M. A. Popović, C. Manolatou, and M. Watts, "Coupling-induced resonance frequency shifts in coupled dielectric multi-cavity filters," Opt. Express **14**(3), 1208–1222 (2006).
9. M. A. Popović, T. Barwicz, M. S. Dahlem, F. Gan, C. W. Holzwarth, P. T. Rakich, H. I. Smith, E. P. Ippen, and F. X. Kärtner, "Tunable, fourth-order silicon microring-resonator add-drop filters," in the 33th European Conference on Optical Communication, ECOC 2007, 1.2.3.
10. J. E. Heebner, V. Wong, A. Schweinsberg, R. W. Boyd, and D. J. Jackson, "Optical transmission characteristics of fiber ring resonators," IEEE J. Quantum Electron. **40**(6), 726–730 (2004).
11. F. Gan, T. Barwicz, M. A. Popovic, M. S. Dahlem, C. W. Holzwarth, P. T. Rakich, H. I. Smith, E. P. Ippen, and F. X. Kartner, "Maximizing the thermo-optic tuning range of silicon photonic structures," in *Photonics in Switching*, 2007, 67–68.
12. N. Sherwood-Droz, H. Wang, L. Chen, B. G. Lee, A. Biberman, K. Bergman, and M. Lipson, "Optical 4x4 hitless slicon router for optical networks-on-chip (NoC)," Opt. Express **16**(20), 15915–15922 (2008).
13. S. T. Chu, B. E. Little, W. Pan, T. Kaneko, and Y. Kokubun, "Cascaded microring resonators for crosstalk reduction and spectrum cleanup in add-drop filters," IEEE Photon. Technol. Lett. **11**(11), 1423–1425 (1999).
14. F. P. Payne and J. P. R. Lacey, "A theoretical analysis of scattering loss from planar optical waveguides," Opt. Quantum Electron. **26**(10), 977–986 (1994).

15. Y. Ding, C. Peucheret, M. Pu, B. Zsigri, J. Seoane, L. Liu, J. Xu, H. Ou, X. Zhang, and D. Huang, "Multi-channel WDM RZ-to-NRZ format conversion at 50 Gbit/s based on single silicon microring resonator," Opt. Express **18**(20), 21121–21130 (2010).
16. Y. A. Vlasov and S. J. McNab, "Losses in single-mode silicon-on-insulator strip waveguides and bends," Opt. Express **12**(8), 1622–1631 (2004).
17. B. E. Little, S. T. Chu, H. A. Haus, J. Foresi, and J. P. Laine, "Microring resonator channel dropping filters," J. Lightwave Technol. **15**(6), 998–1005 (1997).
18. Y. Ding, X. Zhang, X. Zhang, and D. Huang, "Elastic polarization converter based on dual microring resonators," IEEE J. Quantum Electron. **45**(8), 1033–1038 (2009).
19. R. Stoffer, K. R. Hiremath, M. Hammer, L. Prkna, and J. Ctyroky, "Cylindrical integrated optical microresonators: Modeling by 3-D vectorial coupled mode theory," Opt. Commun. **256**(1-3), 46–67 (2005).
20. X. L. Cai, D. X. Huang, and X. L. Zhang, "Numerical analysis of polarization splitter based on vertically coupled microring resonator," Opt. Express **14**(23), 11304–11311 (2006).
21. L. Prkna, M. Hubalek, and J. Ctyroky, "Field modeling of circular microresonators by film mode matching," IEEE J. Sel. Top. Quantum Electron. **11**(1), 217–223 (2005).
22. Y. Cui, Q. Wu, E. Schonbrun, M. Tinker, J.-B. Lee, and W. Park, "Silicon-based 2-D slab photonic crystal TM polarizer at telecommunication wavelength," IEEE Photon. Technol. Lett. **20**(8), 641–643 (2008).

1. Introduction

Optical filters are one of the basic components in modern optical applications, especially in wavelength division multiplexing (WDM) optical networks. An optical bandpass filter (OBPF) is typically applied to filter out the required channel from a WDM signal. An OBPF with high shape factor (SF, defined as the ratio between the −1 dB and −10 dB bandwidths [1]), as well as simultaneous wavelength and bandwidth tunability is much more flexible and preferred, since it can minimize the pulse distortion of the signal, as well as adapt to different bit rates and channels. Wavelength and bandwidth tunability will also be desirable for future dynamic networks. To obtain such bandwidth tunability, several approaches have been proposed and demonstrated so far. For example, a bandwidth-tunable filter based on a single microring resonator (MRR) has been demonstrated by micro-electronic-mechanical-system (MEMS) tuning of the coupling coefficient of the resonator [2,3]. However, to realize MEMS tunability, a high actuation voltage of nearly 40 V should be applied. In another demonstration, the coupling of the MRR was tuned with a Mach-Zehnder interferometer (MZI), resulting in bandwidth tunability of the transmission of the MRR [4]. However, for single MRR schemes, the bandwidth tunability is very limited. Furthermore, as the bandwidth is tuned, the extinction ratio (ER) and the SF of the drop transmission are degraded. To improve the SF and ER, high order MRRs [1,5] and all pass MRR assisted MZI filters [6,7] have also been proposed. The size of the resonators must be carefully designed for high order MRRs due to coupling induced resonance frequency shift (CIFS) [8]. Additionally, thermal controls are introduced for both coupling regions and ring waveguides of each MRR, making the structure relatively complex and hard to control. Wide wavelength tunability filters using high order MRRs have also been investigated [9]. However, their bandwidth is not tunable. A simultaneous wavelength and bandwidth-tunable optical bandpass filter scheme with good SF and ER has not been reported yet.

In this paper, we propose and demonstrate a simple and novel bandwidth and center wavelength-tunable bandpass filter based on a silicon microring-MZI structure. The drop transmissions of two identical MRRs are effectively combined together in the MZI structure. The SF of the Lorentzian response and ER of a single MRR filter are greatly improved by thermally controlling the phase difference between the two arms of the MZI. By thermally tuning the resonance of the two MRRs, both the bandwidth and the center wavelength of the device can be easily linearly tuned over large ranges with good SF, nearly constant ER, and small in-band ripples.

2. Principle of the microring-MZI filter

The proposed device is illustrated in Fig. 1. It consists of two 3 dB splitters and two identical add/drop MRRs. The transmission *t* of the microring-MZI filter can be expressed as [10]

$$t = \frac{1}{2}\left(t_1 e^{j\phi_{MZI}} + t_2\right), \tag{1}$$

$$t_i = -\frac{\kappa^2 \sqrt{a} \exp\left(-j\theta_i/2\right)}{1 - a\left(1 - \kappa^2\right)\exp\left(-j\theta_i\right)}, i = 1, 2, \tag{2}$$

where t_i is the drop transmission of the two MRRs. ϕ_{MZI} is the phase difference between the two arms, which is thermally tuned to π by applying a heating power P_{MZI}. κ is the field coupling coefficient of the coupling region of each MRR. The two MRRs are designed with the same through and drop coupling regions to satisfy the critical coupling condition, so that a minimum insertion loss at the resonance wavelength of the drop port for a single MRR can be obtained, which further leads to an optimized insertion loss of the proposed filter. θ_i and a are the roundtrip phase shift and field transmission coefficient, respectively.
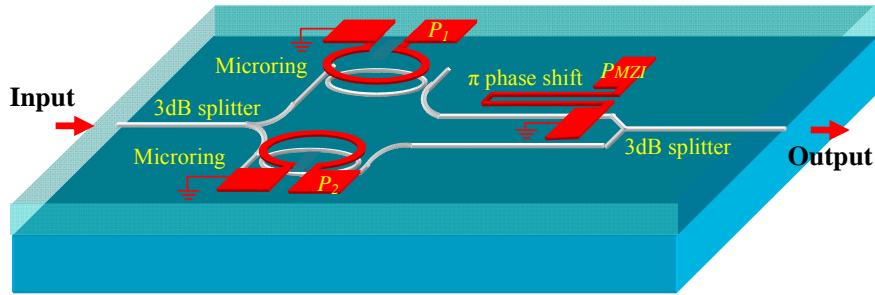

Fig. 1. Structure of the microring-MZI bandwidth and wavelength-tunable bandpass filter. It consists of two 3 dB splitters and two identical MRRs. One heater is added on top of each MRR for resonance offset tuning. Another heater is added on top of one straight waveguide for phase tuning of the MZI.

Figure 2 illustrates the principle of the device. The wavelength-dependent phase shift induced by a single MRR over one free spectral range (FSR) is π. The two drop transmissions t_i are partly overlapped by tuning the resonances of the two MRRs through applying heating powers of P_1 and P_2, respectively. At the wavelength corresponding to the crossing point between the two drop transmissions, a phase shift difference close to π is obtained between the two propagation paths in the MZI. Thanks to the additional π phase shift induced by the heater over the straight section of one MZI arm, the phase shifts of both arms can be made nearly equal, resulting in constructive interference and addition of the two drop transmissions. The bandwidth of the filter can then be tuned by adjusting the resonance offset $\Delta\theta$ between the two drop transmissions. Furthermore, outside the combined passband of the two drop transmissions, the induced extra π phase shift will lead to destructive interference and subtraction of the two drop transmissions, which further improves the SF and ER of the proposed filter. Apart from thermal tuning, carrier injection or carrier depletion in lateral PIN or PN structures can also be used for tuning the resonances of the two MRRs and the phase shift of the MZI. However, thermal tuning is preferred in our application because of its much larger tuning range (~20 nm [11]) compared to that resulting from the free carrier plasma dispersion effect (~2 nm [12]). Furthermore, the fabrication process of a microheater is much simpler than that of the PIN and PN structures.
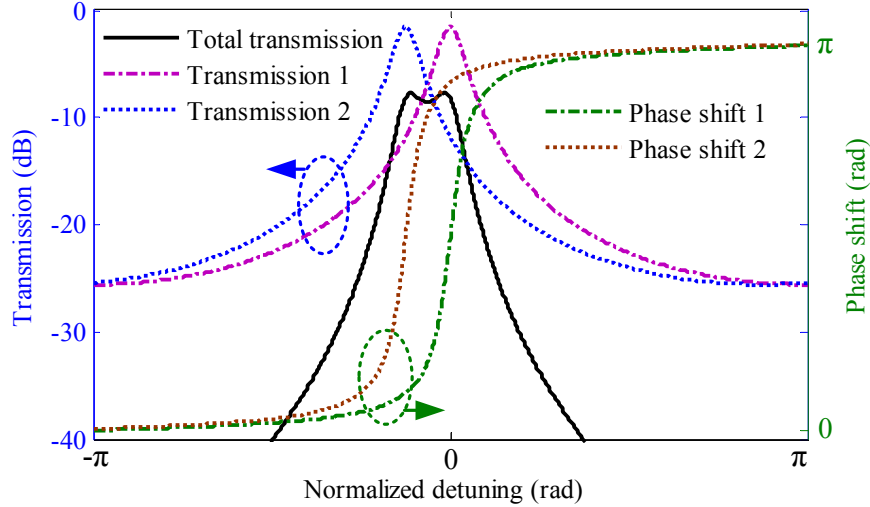
Fig. 2. Principle of the microring-MZI OBPF. Transmissions and phase shifts of the two MRRs, as well as total transmission of the microring-MZI filter. Here parameters $\left|\kappa_1\right|^2 = \left|\kappa_2\right|^2 = 0.1$, $a_1 = a_2 = 0.99$, and $\Delta\theta = \pi/8$ are assumed.

As can be seen in Fig. 2, an in-band ripple results from large resonance offsets. In real applications, the in-band ripple should be as low as possible. For practical applications, in-band ripple below 1 dB is targeted, which limits the maximum bandwidth tunability of the device. On the other hand, the minimum bandwidth tunability is limited by the insertion loss. Figure 3(a) shows the bandwidth (normalized to the bandwidth BW_0 of the drop transmission of a single add/drop MRR; the in-band ripple is kept below 1 dB) tunability and insertion loss as a function of the resonance offset between the two MRRs for different power coupling coefficients of the MRRs. One can find that, for different coupling conditions, as the resonance offset increases, the insertion loss decreases and will converge to a minimum value, which is introduced by the two 3 dB splitters as well as the loss of the ring waveguide. To ensure minimum insertion loss, the resonance offset cannot be too small, which will determine the minimum attainable bandwidth. The effective resonance offset is defined as the range where the insertion loss degrades less than 1 dB from the minimum value and the in-band ripple is kept below 1 dB. As shown in Fig. 3(a), in the effective resonance offset range, the bandwidth can be tuned from $1 \times BW_0$ to more than $2.2 \times BW_0$. Figure 3(b) shows the ER and SF as a function of the resonance offset between the two MRRs in the effective resonance offset range for different power coupling coefficients. One can find that the ER decreases as the resonance offset increases. For lower power coupling coefficients, the ER performance is better. On the other hand, for all the coupling conditions, the SF increases fast as the resonance offset increases. The highest SF can reach up to about 5.5, which is comparable with that of third order cascaded MRRs [1]. The filter response for different roundtrip field transmission coefficients a is also investigated. As shown in Figs. 3(c) and 3(d), an increase of a can improve the insertion loss and ER of the filter. This is because when a increases, less light is lost in the MRR, resulting in higher field enhancement in the MRR and increased power output from the drop port, thus leading to an improvement of the insertion loss of the filter. Furthermore, from Eq. (2), the ER of a single MRR can be expressed as $ER_i = 20\log_{10}\left\{\left[1+a\left(1-\kappa^2\right)\right]/\left[1-a\left(1-\kappa^2\right)\right]\right\}$. One can find that an increase of a will lead to a higher ER of the drop transmission of the MRR, and will further improve the ER of the filter. However, the increase of a does not improve the normalized bandwidth tunability and SF performance. Even though an increase of a leads to a narrower bandwidth of the MRR,

the effective resonance offset range of the filter decreases. Hence the normalized bandwidth tunability and SF keep unimproved in the effective resonance offset range.

In Table 1, we summarize the performances of different MRR-based OBPF schemes. Although the SF of our device is lower than that of the all-pass MRR assisted MZI structure, it is still better than that of the second order MRR structure, and comparable with that of the third order MRR structure. Additionally, the simultaneous bandwidth and wavelength tunability makes it even more attractive.
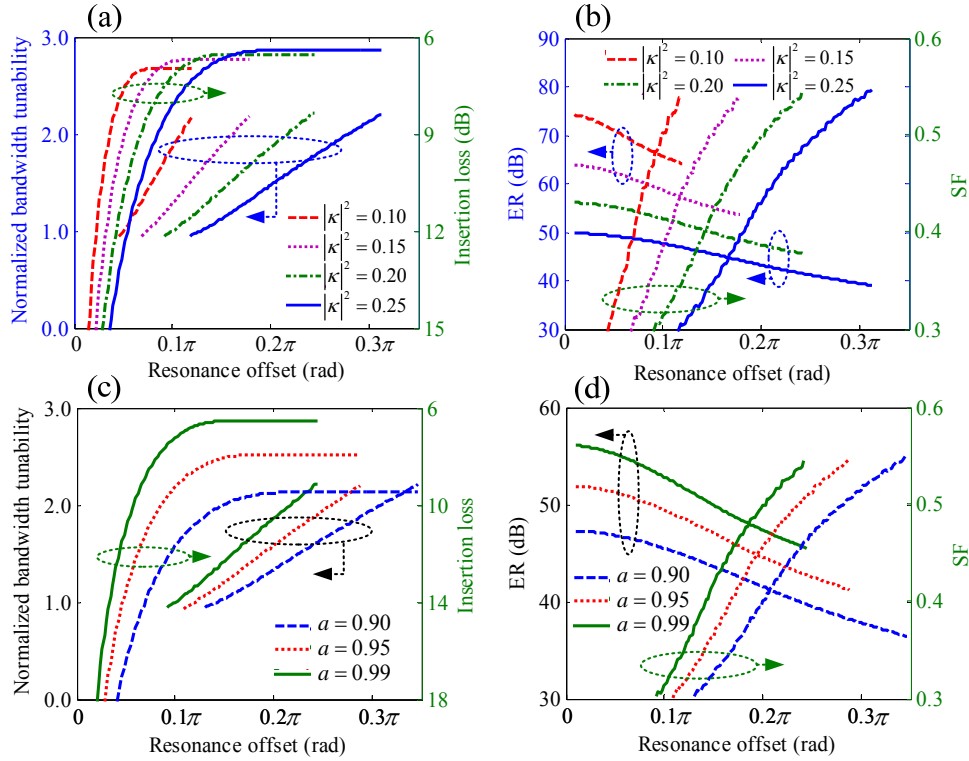
Fig. 3. Left: Normalized bandwidth tunability and insertion loss as a function of the resonance offset for (a) different power coupling coefficients with $a = 0.99$ and (c) different roundtrip field transmission coefficients a with $|\kappa|^2 = 0.20$. Right: ER and SF as a function of the resonance offset (in the effective resonance offset range) for (b) different power coupling coefficients with $a = 0.99$ and (d) different roundtrip field transmission coefficients a with $|\kappa|^2 = 0.20$.

Table 1. Comparison of Different Types of MRR-based OBPFs.

Filter Type	ER	SF	Bandwidth Tunability	Wavelength Tunability
First order MRR [13]	20 dB	0.17	No	Not demonstrated
Second order MRR [13]	20 dB	0.40	No	Not demonstrated
Third order MRR [1]	40 dB	0.55	No	Not demonstrated
All-pass MRR assisted MZI [6]	30 dB	0.75	Not demonstrated	Not demonstrated
This work	30 dB	0.55	Yes	Yes

3. Design and fabrication

As an application of the principles described in the previous section, our goal is to demonstrate a bandwidth and wavelength-tunable filter centered around 1550 nm with

bandwidth-tunable range of 0.32 nm to 0.8 nm. According to the previous analysis, the bandwidth BW_0 of the drop transmission of a single add/drop MRR should be about 0.32 nm. A silicon-on-insulator (SOI) wafer with top silicon layer of 250 nm is selected for the design. The design radius R of the MRR is 10 μm. The cross section of the waveguide is designed as illustrated in Fig. 4(a). The waveguide width and height are designed to be 430 nm and 250 nm, respectively. A layer of benzocyclobutene (BCB) is used to cover the waveguide and form the upper cladding layer. A 100 nm Ti with 5 nm Au heater is deposited on top of the BCB for thermal tuning. To minimize the crosstalk between TE and TM modes, the device is designed for TM mode operation (Fig. 4(b)), since the coupling for the TE mode is much smaller in our design. By extending the 2D planar waveguide model [14] to 3D waveguide structures [15], the scattering loss is evaluated to be 3.1 dB/cm when calculated using the mode profile (Fig. 4(b)) associated with typical sidewall roughness standard deviation σ of 3 nm and its correlation length L_c of 50 nm [16] for the designed waveguide structure.

Considering the relationship between BW_0 and $|\kappa|^2$ according to $BW_0 = 2|\kappa|^2 \lambda^2 / \left[(2\pi)^2 Rn_{eff} \right]$ [17], n_{eff} being the effective index of the designed waveguide, a bandwidth BW_0 of 0.32 nm is obtained for a single add/drop MRR, provided the power coupling coefficient $|\kappa|^2$ is equal to 5.2%, corresponding to a coupling gap of 410 nm (calculated by the coupled mode theory according to [18,19]).
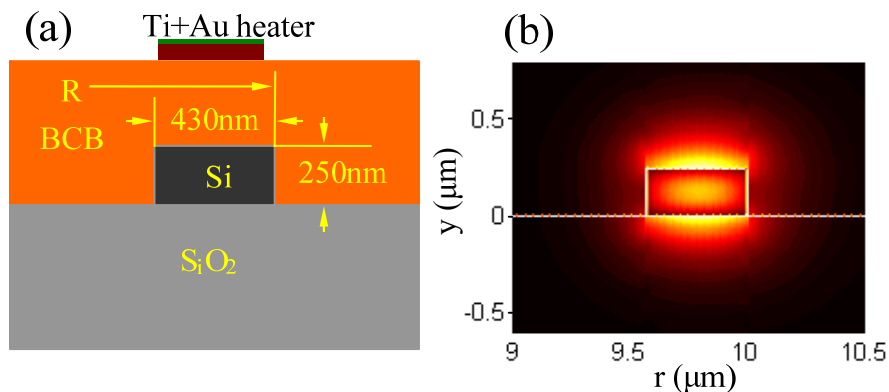

Fig. 4. (a) Cross section of the designed waveguide and (b) corresponding TM_0 mode profile of the electric field calculated by the full vectorial mode matching method [20,21].

Figure 5 shows pictures of the fabricated device. The device is fabricated on a SOI wafer with top silicon thickness of 250 nm and buried silicon dioxide of 3 μm. Diluted (1:1 in anisole) electron-beam resist ZEP520A is spin-coated on the wafer to form a ~110 nm-thick mask layer. The microring-MZI structure is then defined using electron-beam lithography (JEOL JBX-9300FS). After that, the sample is etched by inductively coupled plasma reactive ion etching (ICP-RIE) to transfer the patterns to the top silicon layer. Afterwards, a top cladding layer of 550 nm BCB is spin-coated for planarization, and a layer of 400 nm ZEP520A is spin-coated in sequence as the mask layer for the heaters. Electron-beam lithography is used again to define the patterns of the heaters and pads. Finally, heaters and pads (100 nm thick titanium with 5 nm thick Au) are formed by evaporation and lift-off techniques. The radii of the two MRRs are 10 μm, with waveguide width of 435 nm and coupling gap of 402 nm for both through and drop coupling regions, as shown in Fig. 5(a).
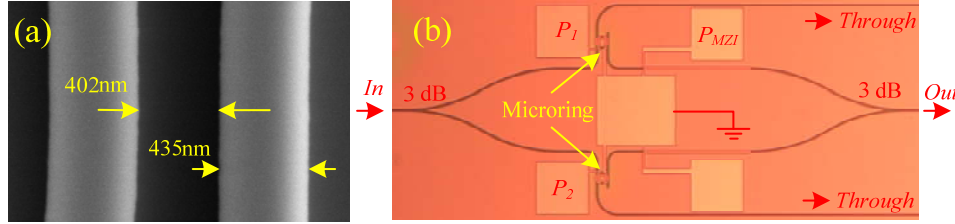
Fig. 5. (a) Scanning electron microscope (SEM) top view image of the coupling region of the MRR. (b) Optical microscope picture of the fabricated device. Two identical add-drop MRRs with micro-heaters are inserted in the two arms of the MZI structure. Heating powers of P_1 and P_2, are applied to the MRR heaters, while an heating power of P_{MZI} is applied to one of the heaters deposited on top of the straight sections of the MZI.

4. Experimental results

4.1 SF and ER improvement

Figure 6(a) shows the measured through transmission of a single MRR at the through port, as shown in Fig. 5(b). Note that the transmission is normalized to that of a straight waveguide with the same cross section. Around 3.6 dB insertion loss is obtained because of the 3 dB splitter as shown in Fig. 5(b). By fitting the measured through transmission, a power coupling coefficient of 5.5% is obtained, which agrees well with the design. However, a fitted roundtrip field transmission coefficient a of 0.92 (corresponding to a propagation loss of 120 dB/cm) is obtained, which deviates significantly from the estimated scattering loss. This is potentially due to the excess loss induced by the metal heater. From Fig. 4(b), one can find that the field distribution of the TM_0 mode of the designed waveguide extends beyond 600 nm above the waveguide in the upper cladding layer. Since the top cladding layer is only 550 nm thick, the field overlaps with the metal heater, leading to a large propagation loss. Figure 6(b) shows the measured transmissions for the TM mode of the fabricated device. When $\phi_{MZI} = 0$ ($P_{MZI} = 0$ mW), the transmission of the device almost has a Lorentzian-shape with low ER. Using the fitted power coupling coefficient and a from Fig. 6(a), the calculated filter response shows good agreement with the measured transmission, as shown in Fig. 6(b). As predicted in the previous analysis, when $\phi_{MZI} = \pi$ ($P_{MZI} = 11.6$ mW), the ER is greatly improved to 30 dB. Moreover, the SF is also significantly improved to a value of 0.43, with −1 dB and −10 dB bandwidths of 0.52 nm and 1.2 nm, respectively. An insertion loss of 15 dB is measured, which is due to the large propagation loss as analyzed before. However, the insertion loss can be greatly improved using a thicker top cladding layer in order to reduce the propagation loss induced by the metal heater.
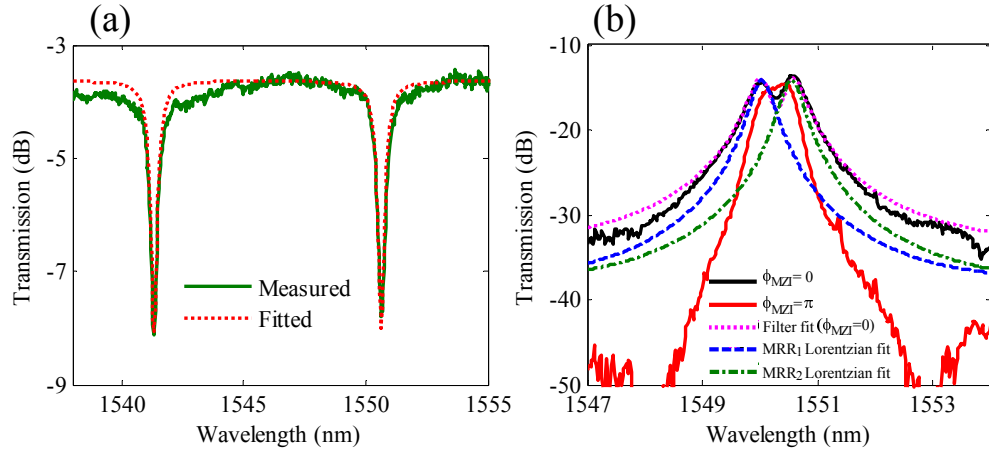
Fig. 6. (a) Measured and fitted through transmission, which is normalized to a straight waveguide, of a single MRR. (b) Measured transfer functions showing SF and ER improvement at $\phi_{MZI} = \pi$ ($P_{MZI} = 11.6$ mW) compared to the Lorentzian-shapes at $\phi_{MZI} = 0$ ($P_{MZI} = 0$ mW). Lorentzian fits of the transmissions of the two MRRs, as well as the filter are also represented.

4.2 Bandwidth tunability

Figure 7 shows the measured 3 dB bandwidth tunability (for an in-band ripple smaller than 1 dB) of the fabricated device working on TM mode. The heating power of the MZI arm is kept to 11.6 mW to maintain a π phase difference between the two MZI arms. Both P_1 and P_2 are adjusted to preserve the centre wavelength. One can find that, by applying different heating powers to the two MRRs, the resonance offset is effectively tuned, resulting in tuning of the bandwidth, as shown in Fig. 7(a). The 3 dB bandwidth can be linearly tuned by P_1 from 0.46 nm to 0.88 nm, which almost agrees with the design, as illustrated in Fig. 7(b). About 30 dB ER is obtained. The SF increases with increasing bandwidth, which also agrees with the simulations. However, a drop of the SF for $P_1 = 0.88$ mW and $P_2 = 4.14$ mW is observed, which is deteriorated by the imperfect splitting ratio of the 3 dB splitter.
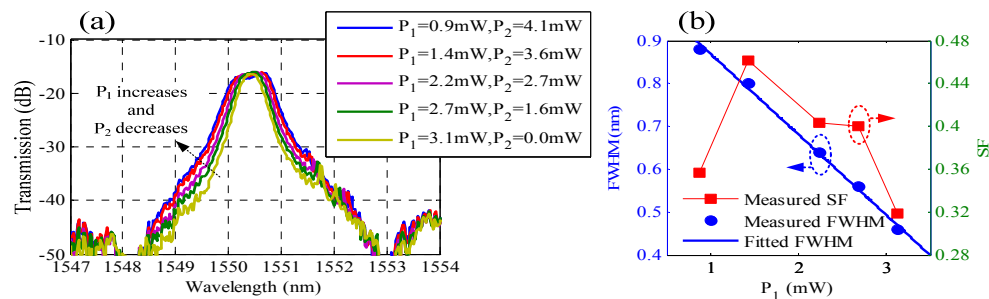

Fig. 7. (a) Measured bandwidth tunability of the fabricated device for in-band ripple smaller than 1 dB. The straight waveguide heating power is $P_{MZI} = 11.6$ mW . (b) FWHM bandwidth and shape factor of the filter as a function of the heating power applied to one of the MRRs.

4.3 Wavelength tunability

Figure 8 represents the wavelength tunability (for in-band ripple smaller than 1 dB) of the fabricated device working on TM mode. The heating power of the MZI arm is still 11.6 mW to keep a π phase difference between the two MZI arms. Both P_1 and P_2 are adjusted so that the shape of the filter keeps unchanged during the wavelength tuning. As shown in Fig. 8(a),

the center wavelength of the passband is tuned by tuning the heating powers applied to the two MRRs. The center wavelength evolution as a function of the heating power P_1, which can be seen to be linear from 1550 to 1554 nm, is represented in Fig. 8(b). The wavelength tunability can be further improved by using SiO_2 or hydrogen silsesquioxane (HSQ) as the top cladding layer instead of BCB, due to their better thermal conductivity. The SF is also monitored during the wavelength tuning. One can find that the SF can be kept around 0.33~0.5, without notable degradation during the wavelength tuning. Due to the imperfect TE mode extinction of the polarization controller, there remains some residual TE mode light. Such TE crosstalk can be released by introducing a polarizer, for instance a photonic crystal, after the microring-MZI to block the TE mode light [22].
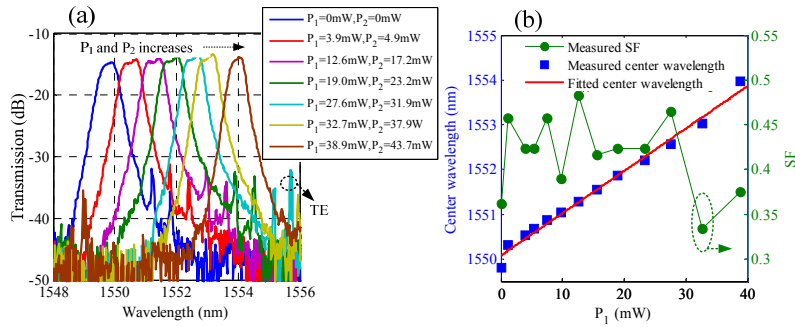
Fig. 8. (a) Transmission of the device for different heating powers combinations applied to the two MRRs, showing the center wavelength tunability. (b) Evolution of the center wavelength of the passband as a function of heating powers, as well as SF measured when tuning the wavelength. Only transfer functions with in-band ripple smaller than 1 dB are considered. The straight arm heating power is $P_{MZI} = 11.6\text{mW}$.

5. Conclusion

We have proposed and demonstrated a bandwidth and wavelength-tunable OBPF based on a silicon microring-MZI structure. An effective bandwidth tuning range from 0.46 to 0.88 nm, and wavelength tuning range from 1550 to 1554 nm are demonstrated experimentally with proper adjustment of the heating powers applied to the two MRRs and the straight section of the MZI. Good ER and SF are also obtained for the device. Due to its CMOS-compatible fabrication process, compact size, good ER and SF performances, and flexible bandwidth and wavelength tunability, our scheme is very promising for practical implementations.

Acknowledgments